Flexible Neural Interfaces Based on 3D PEDOT:PSS Micropillar Arrays

Alice Lunghi, Anna Mariano, Michele Bianchi, Nikita Bhupesh Dinger,
Mauro Murgia, Eliana Rondanina, Andrea Toma, Pierpaolo Greco, Michele Di Lauro,
Francesca Santoro,* Luciano Fadiga, and Fabio Biscarini*

Multi-electrode arrays with 3D micropillars allow the recording of electrophysiological signals in vitro with higher precision and signal-to-noise ratio than planar arrays. This is the result of the tight interaction between the 3D electrode and the cell membrane. Most 3D electrodes are manufactured on rigid substrates and their integration on flexible substrates is largely unexplored. Here, a straightforward approach is presented for fabricating soft interfaces featuring 3D poly(3,4-ethylenedioxythiophene)-poly(styrenesulfonate) (PEDOT:PSS) micropillars on a soft flexible substrate made of polydimethylsiloxane (PDMS). Large-area isotropic arrays of PEDOT:PSS micropillars with tailored geometric area, surface properties, and electrochemical characteristics are fabricated via a combination of soft-lithography and electrodeposition. A 60% increase in capacitance is achieved for high density micropillars compared to planar electrodes and this is found to be correlated with the increased electroactive surface area. Furthermore, 3D PEDOT:PSS micropillars support adhesion, growth and differentiation of SH-SY5Y cells, and influence the direction of neurite outgrowth. Finally, by virtue of their elasticity, soft micropillars act as excellent anchoring loci for elongating neurites, facilitating their bending and twisting around the micropillar, increasing the number of contact points between the cells and the electrode, a key requirement to obtain high performance neural interfaces.

1. Introduction

In vitro multi-electrode arrays (MEAs) represent the state-of-the art for the recording and stimulation of the electrophysiological activity of electrogenic neural and cardiac cells.[1–3] MEAs more often consist of planar electrodes (tens to hundreds) that allow parallel and simultaneous detection of spontaneous or evoked local field potentials.[3,4] In order to record high-fidelity and good-quality electric signals, several topography-based biomimetic approaches were recently developed to improve the physical and electrical coupling between cells and electrodes.[5–9] For instance, 3D mushroom-shaped microelectrodes were used by Hai et al. to record "intracellular-like" signals and subthreshold synaptic potentials[10] and 3D nanoelectrodes were employed to record intracellular action potentials.[11–14] In addition, 3D micropillars were used to measure cellular traction forces, study cell-extracellular matrix (ECM) interaction, or deliver electrical

A. Lunghi, M. Bianchi, M. Murgia, P. Greco, M. Di Lauro,
L. Fadiga, F. Biscarini
Center for Translational Neurophysiology of Speech and Communication
Fondazione Istituto. Italiano di Tecnologia
via Fossato di Mortara 17, Ferrara 44121, Italy
E-mail: michele.bianchi@iit.it

A. Lunghi, P. Greco, L. Fadiga
Sezione di Fisiologia
Università di Ferrara
via Fossato di Mortara 17, Ferrara 44121, Italy

A. Mariano, N. B. Dinger, F. Santoro
Tissue Electronics
Istituto Italiano di Tecnologia
Naples 80125, Italy
E-mail: francesca.santoro@iit.it

N. B. Dinger
Dipartimento di Chimica
Materiali e Produzione Industriale
Università di Napoli Federico II
Naples 80125, Italy

M. Murgia
Institute for Nanostructured Materials (ISMN)
Consiglio Nazionale delle Ricerche
via Gobetti 101, Bologna 40129, Italy

E. Rondanina, A. Toma
Clean Room Facility
Fondazione Istituto Italiano di Tecnologia
via Morego 30, Genoa 16163, Italy

F. Santoro
Faculty of Electrical Engineering and Information Technology
RWTH Aachen
52074 North Rhine-Westphalia, Germany

2200709 (1 of 11)

or mechanical signals.[15] Despite MEA's capability to acquire multiplexed electrophysiological recordings, Young's elastic modulus and bending stiffness of the materials commonly used as electrodes (Au, Pt, IrOx) are much higher than that of cells.[16–18] This mechanical mismatch at the cell–material interface can hinder both physical and electrical coupling, compromising the overall quality of the recorded signal.[19,20] The use of conducting polymers in neuroelectronics has proven effective for increasing the signal-to-noise ratio (SNR) of the recorded signals.[5,21,22] Indeed, conjugated polymers can offer at the same time appropriate mechanical properties, high electrochemical capacitance and mixed ionic-electronic conduction,[23] all desired properties when interfacing electrical devices with living systems.[5] Besides, conjugated polymers conducting properties also offer advantages for stimulation of the neuronal activity, thanks to the larger charge storage capacity and lower charge injection limit when compared to metal electrodes.[24–30] The fabrication by soft-lithography of cone-shaped poly(3-hexylthiophene-2,5-diyl) microstructures on glass was recently reported, enabling the establishment of a close contact with the neuronal cell membrane, without negatively affecting cell viability and electrophysiological properties,[31] as well as to direct neurite outgrowth.[32]

In order to reduce this mechanical discrepancy at the cell–material interface, soft 3D micropillar arrays of poly(3,4-ethylenedioxythiophene)-poly(styrenesulfonate) (PEDOT:PSS) hydrogel-coated IrOx electrodes have been developed by Liu et al. Here, the soft PEDOT:PSS hydrogel micropillars promoted a tighter interaction with cardiomyocytes, and the lower impedance of the conducting polymer, compared to the metal oxide electrode, enabled the recording of large amplitude action potentials.[33]

The integration of conductive 3D microstructures into flexible and biocompatible substrates such as polydimethylsiloxane (PDMS)[34–36] and polyurethane (PU)[36] based elastomers or biodegradable polymers such as polylactic acid (PLA) and polyglycolic acid (PLGA),[37,38] is crucial in the development of advanced 3D neural devices for both chronic and acute in vivo applications.[39,40] In order to develop implantable and/or wearable devices, including biosensors, brain–machine interfaces and neural prosthetics or soft conductive scaffolds for neural repair strategies, MEAs flexibility and stretchability become of paramount importance to increase device conformability as well as reducing the immune foreign-body response.[41,42]

Here, we report a straightforward approach for the fabrication of PEDOT:PSS micropillars on a highly flexible substrate such as PDMS. Initially, the multiscale morphology and electrochemical properties of PEDOT:PSS-coated PDMS micropillars of different sizes and pitches (hereinafter referred to as 3D_PEDOT) were investigated. The viability and differentiation of SH-SY5Y neuroblastoma cells cultured on 3D_PEDOT was evaluated, to assess the capability of the soft conductive micropillars to support neural cell adhesion and differentiation as well as to influence neurite outgrowth direction. Our results represent an important step toward the design of soft bioelectronics interfaces in a rapid prototyping approach combining soft-lithography and electrodeposition.

2. Results and Discussion

2.1. Fabrication and Morphological Characterization of the 3D_PEDOT Arrays

The fabrication process of the soft 3D_PEDOT arrays is outlined in **Figure 1**a. Representative scanning electron microscopy (SEM) images of the silicon master featuring microholes, the PDMS replica exhibiting micropillars, the metallized PDMS replica, and the final PEDOT:PSS micropillars are shown in Figure 1b–e. The periodicity of the 3D_PEDOT array is highlighted by the 2D-Fast Fourier Transform (FFT) of large-scale optical images in Figure S1, Supporting Information.

Silicon masters were designed to feature microholes upon ion etching treatment. Previous studies have demonstrated the potential of low aspect ratio micropillar arrays to create a biomimetic permissive environment that would support neurons growth and encourage neurite elongation.[16,43] Therefore, the nominal diameter of microholes in the mask was designed to be 5 µm for samples labelled as A and 7 µm for samples labelled as B. However, the final mean hole diameters obtained upon ion etching of the silicon masters were 6.7 and 8.3 µm for A and B, respectively (Figure 1b and Table S1, Supporting Information). The mean depth of the microholes was 3 µm. As a result, the aspect ratio (i.e., height to diameter ratio) ranged from 0.4 to 0.5 (Table S1, Supporting Information). For both A and B, the interpillar distance of 15 and 30 µm, therefore obtaining two arrays with a 15 µm pitch (A_15 and B_15) and arrays with a 30 µm pitch (A_30 and B_30).

PDMS micropillars where then obtained by replica molding (Figure 1c); their diameter, height, and aspect ratio are reported in Table S1, Supporting Information. As expected, A_15 and B_15 PDMS micropillar arrays showed a 30–35% increase in surface area compared to flat PDMS substrates, whereas the surface area increases for A_30 and B_30 compared to flat PDMS was only 7–9% owing to the bigger interpillar distance (Table S1, Supporting Information).

After a thin Ti−Au layer was thermally evaporated on the PDMS substrates (38 nm, Figure S2, Supporting Information), PEDOT:PSS thin films were deposited on the PDMS micropillars surface by electrochemical deposition. Representative scanning electron and atomic force micrographs are reported in Figure 1e and **Figure 2**, respectively.

PEDOT:PSS micropillars diameter, height, and aspect ratio are like those measured for PDMS micropillars (Table S2, Supporting Information), suggesting that the thin layer of PEDOT:PSS (300–400 nm) homogeneously grew both on the top of and between pillars (Figure 2b). Interestingly, the deposition of the polymer layer increased the surface roughness from ≈0.3 nm (RMS$_{PMDS}$ calculated on a 5×5 µm^2 length scale,

F. Santoro
Institute for Biological Information Processing-Bioelectronics
IBI-3
Forschungszentrum Juelich
52428 Jülich, Germany

F. Biscarini
Life Science Department
Università di Modena e Reggio Emilia
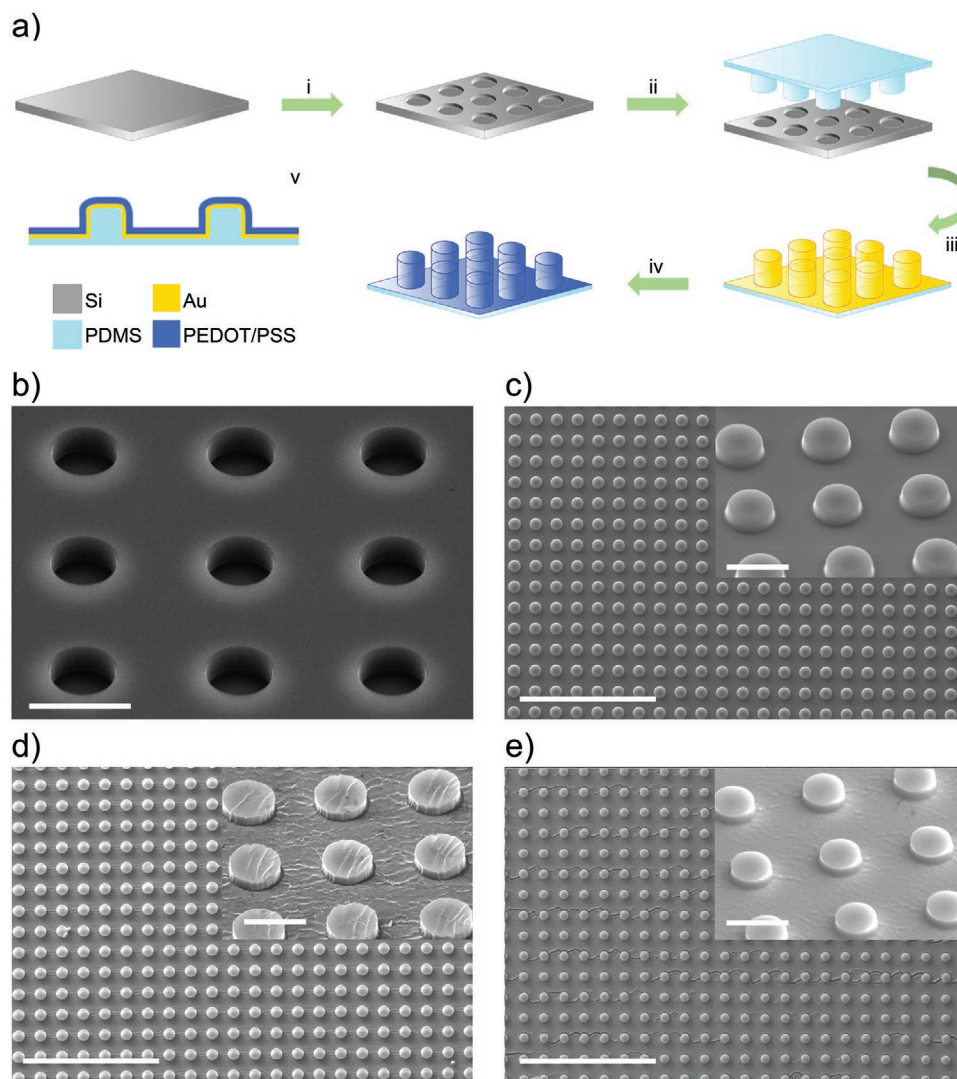via Campi 103, Modena 41125, Italy

**ADVANCED
SCIENCE NEWS**

www.advancedsciencenews.com

**ADVANCED
MATERIALS
INTERFACES**

www.advmatinterfaces.de

Figure 1. PEDOT:PSS micropillars fabrication process. a) A schematic representation of the fabrication steps depicting: i) ion etching of the Si master featuring microholes; ii) replica molding of the master micro-holes to obtain PDMS micropillars; iii) metallization of the PDMS substrates with Ti−Au; iv) electrochemical deposition of the PEDOT:PSS layer; and v) a schematic drawing showing the section of a final 3D_PEDOT electrode (not in scale). Scanning electron micrographs of b) the Si master, c) the PDMS replica (B_15), d) the metallized PDMS replica (B_15), and e) the final 3D_PEDOT electrode (A_15). Scale bar in (b) is 10 μm, in (c–e) is 100 μm; scale bar of the insets in (c–e) is 10 μm.

Figure S2, Supporting Information) to ≈15 nm (RMS$_{PEDOT:PSS}$, calculated on the same length scale). This is ascribed to the nucleation of PEDOT:PSS grains with an average diameter of ≈60 nm (Figure 2c).[44]

To further characterize surface properties of the substrates, characteristic water contact angle values for PDMS, and metallized PDMS and 3D_PEDOT were measured (Figure S3, Supporting Information). PDMS and Au-coated PDMS substrates exhibited a high hydrophobic surface (w contact angle 90° < θ < 120°, Figure 2d), while the addition of the thin PEDOT:PSS layer dramatically improved the wettability of the electrode, decreasing the contact angle to values compatible with cell adhesion (contact angle 50° < θ < 80°, Figure 2d-i–v).[45–47] As expected, the wettability of A_15 and B_15 was lower than that of A_30 and B_30, respectively (Figure 2d-i–v), suggesting that the higher pillar density contributes to higher hydrophobicity.

Microcracks were observed in both Au-coated PDMS and in 3D_PEDOT and their formation is probably ascribed to the mechanical mismatch between the gold coatings and the elastic PDMS substrate underneath (Figure 1d,e).[48] Interestingly, the presence of the pillars decreased number of cracks and their length compared to flat samples (Figures S6 and S7, Supporting Information), as also previously reported for Au-coated PDMS substrates.[49] However, the presence of cracks did not affect electrodes' conductivity or electrochemical properties.

2.2. Electrochemical Characterization of the 3D_PEDOT Arrays

Characteristic parameters (i.e., the onset potential, the solution resistance, and the impedance modulus) of the electrodeposition process and electrochemical characterization are reported
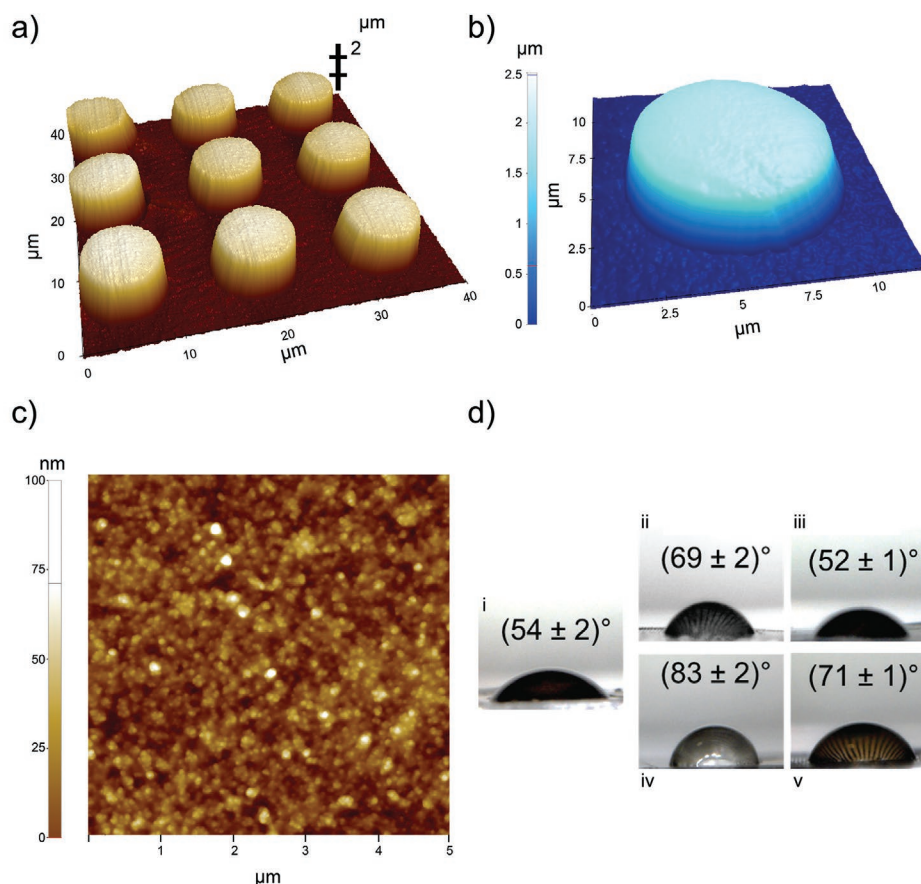
2200709 (3 of 11)

**ADVANCED
SCIENCE NEWS**
www.advancedsciencenews.com

**ADVANCED
MATERIALS
INTERFACES**
www.advmatinterfaces.de

Figure 2. Surface characterization of 3D_PEDOT electrodes. a) 3D AFM topography image of an array of PEDOT:PSS micropillars. b) 3D AFM topography image of a single micropillar from a 3D_PEDOT electrode. c) 2D AFM topography image of the surface of the PEDOT:PSS layer from a 3D_PEDOT electrode. Top of the pillars and bottom space showed similar RMS a grain size. d) Water contact angles for i) flat, ii) A_15, iii) A_30, iv) B_15, and v) B_30.

in Table S3, Supporting Information. Here, while the oxidation potential of the EDOT monomer was similar for all electrodes at the first cycle (ca. 0.950 mV),[26] the peak current during the last (15th) cycle varied across substrates in the 80 ÷ 110 µA range (**Figure 3**a). In fact, the oxidation potential is mainly influenced by the solvent and the counter ion which were both kept constant. It is also known that the current exchanged during the deposition is correlated to the area of the working electrode,[50] which here varied across samples (Table S1, Supporting Information), resulting in electrodeposited PEDOT:PSS films of different thicknesses (Table S2, Supporting Information).

The Bode plot of PEDOT:PSS coated electrodes (Figure 3b) is characterized by a large frequency independent region at higher frequencies and a progressive increase of the impedance at lower frequencies. This is due to the mixed ionic-to-electronic conductance of PEDOT:PSS.[51] In particular, the Bode plot indicates a nearly 3-orders-of-magnitude drop of the impedance at low frequency (0.5 Hz) for PEDOT-coated substrates compared to uncoated ones, in agreement with previous findings comparing PEDOT-coated with pristine metallic microelectrodes.[21] The modulus |Z| measured at 1 kHz is commonly used to estimate the thermal noise level of the system during neural recordings[52] and here varies from 900 to 140 Ω (PEDOT-coated Au/PDMS). A_15 and B_15 electrodes showed slightly

lower impedance across all the investigated frequency ranges compared to A_30 and B_30 (Figure 3c). In particular B_15, in virtue of the higher geometric area and PEDOT:PSS coating thickness, showed the lowest impedance values across all the frequency spectrum (Table S3, Supporting Information).

We then measured the double layer capacitance of the 3D_PEDOT by cyclic voltammetry (for further details see the Experimental Section and Figure S4a,b, Supporting Information). The presence of micropillars significantly increased the electrode capacitance compared to flat PEDOT:PSS (Figure 3d). In particular B_15 showed the highest increase in capacitance (62%) compared to flat PEDOT:PSS. Furthermore, the capacitance of both A_15 and B_15 was higher compared to A_30 and B_30.

Finally, we evaluated the electroactive surface area (ESA) which provides a real quantification of the amount of polymer contributing to the double layer capacitance.[53] ESA values were obtained by means of cyclic voltammetry in the presence of an appropriate redox couple (Figure S4c,d, Supporting Information). B_15 electrodes exhibited the highest ESA (Figure 3e) and this was similar to what was observed for the double layer capacitance. In agreement with previous reports,[53] the double layer capacitance and the ESA, were highly correlated (Figure 3f).
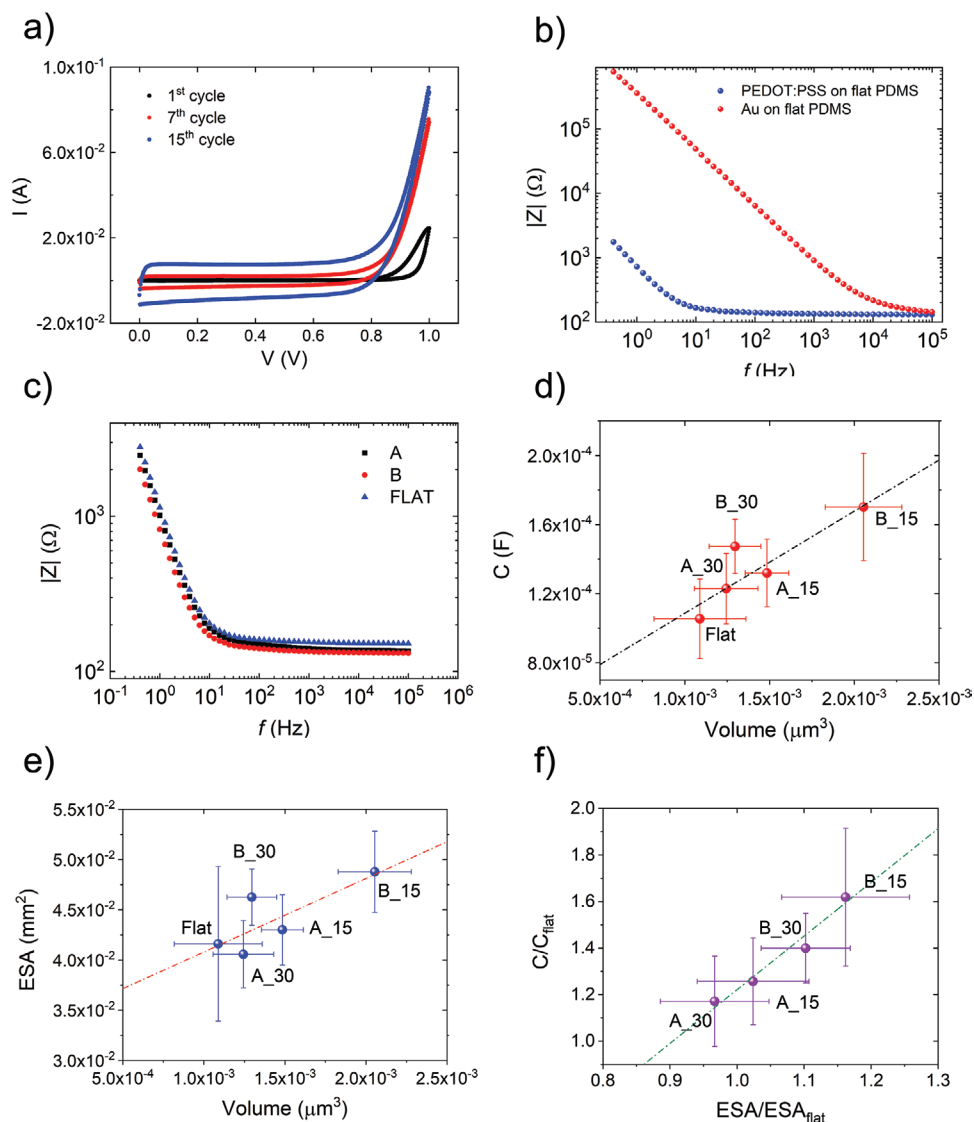
**ADVANCED
SCIENCE NEWS**

www.advancedsciencenews.com

**ADVANCED
MATERIALS
INTERFACES**

www.advmatinterfaces.de

Figure 3. Electrochemical characterization of 3D_PEDOT arrays. a) Exemplary electrodeposition curves (1st, 7th, and 15th cycle) of 3D_PEDOT. b) Bode plot of Au/flat PDMS versus PEDOT:PSS-coated Au on flat PDMS. c) Bode plot of 3D_PEDOT compared to PEDOT:PSS-coated flat PDMS. d) Capacitance C and e) electroactive surface area ESA of 3D_PEDOT versus electrode volume. f) Correlation plot between the normalized capacitance (C/C_{flat}) and the normalized ESA (ESA/ESA_{flat}). In (d–f), dot-dashed lines are linear fit ($R^2 = 0.85$, 0.73, and 0.97, respectively).

These results confirm that the areal capacitance (C_A, C/ESA) is a relevant material's property for PEDOT:PSS electrodes. Interestingly, C_A of the electrodeposited PEDOT:PSS layer was (69 ± 14) F cm^{-2}, ≈70 times higher than the same property for spin coatings.[53] We propose that this enhanced capacitance arises from the different microstructures of PEDOT:PSS films deposited according to the two methods, being denser than that of PEDOT made by spin coating, and more porous than that obtained by electrodeposition, therefore more prone to electrolyte penetration and to double layer setting up.

In summary, the addition of the PEDOT:PSS layer provided a flexible interface showing significantly lower impedance and higher capacitance compared to the metallized PDMS micropillars, and a more suited interface for neural cell adhesion, thanks to the presence of a rough and moderately hydrophilic surface.

2.3. Evaluation of SH-SY5Y Cell Viability and Differentiation on 3D_PEDOT Arrays

In order to assess the biocompatibility of PEDOT:PSS micropillar arrays with SH-SY5Y cells, a live/dead fluorescence assay was performed after 1 day in vitro (DIV). The green fluorescent signal of live cells labelled with Calcein-AM and the red fluorescent signal of dead cells labelled with ethidium homodimer (**Figure 4**a) were used to quantify cell viability as shown in Figure 4b. SH-SY5Y cells displayed excellent viability on PEDOT:PPS (both micropillar and flat electrodes), with a high percentage of live cells (above 95%) comparable to the percentage measured for glass control samples. Furthermore, no significant difference in the percentage of live cells was found across substrates, suggesting that they all display negligible cytotoxic effects irrespective of the material or
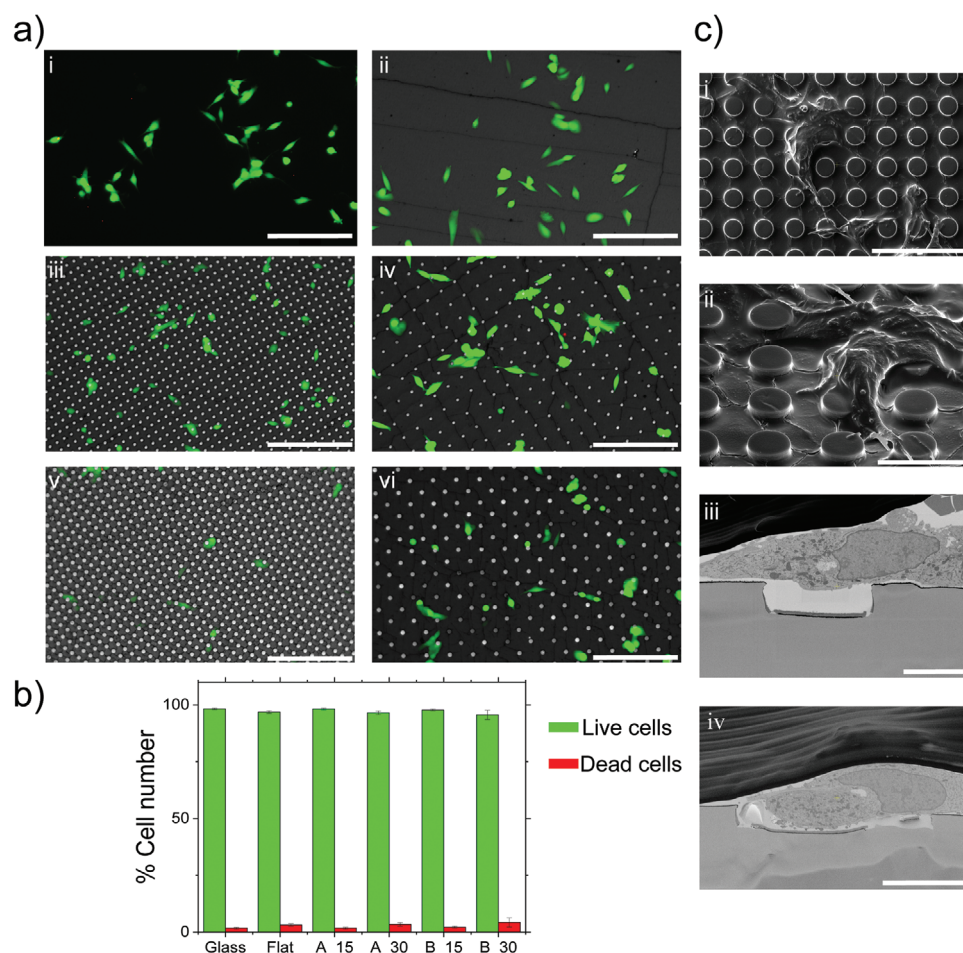
**ADVANCED
SCIENCE NEWS**

www.advancedsciencenews.com

**ADVANCED
MATERIALS
INTERFACES**

www.advmatinterfaces.de

Figure 4. The effect of PEDOT:PSS micropillars on SH-SY5Y cells viability. a) Cell viability assay showing fluorescently labelled live (green) and dead (red) cells on glass (i), flat (ii), A_15 (iii), A_30 (iv), B_15 (v), and B_30 (vi). Scale bar 150 μm. b) Percentage of live and dead cell reported as mean ± SEM (*n* = 3). c) Scanning electron micrographs showing top-view (i) and tilted view of differentiated SH-SY5Y cells on B_15. i) Scale bar 50 μm. ii) Scale bar 20 μm. iii) B_15-cell cross section. Scale bar 5 μm. iv) B_30-cell cross section. Scale bar 10 μm. Red dashed lines in (iii) and (iv) show the micropillars cross section profile.

micropillars size and pitch. These results agree with previous works on PEDOT:PSS biocompatibility[54,55] and highlight how the micropillars aspect-ratio neither causes relevant damage to cells' integrity nor cell death. Scanning electron micrographs showed that PEDOT:PSS micropillars foster both cell adhesion and spreading of either undifferentiated (Figure S5, Supporting Information) or differentiated SH-SY5Y cells (Figure 4c-i,ii). Top-view and tilted micrographs show the formation of protrusions at the cell–material interface extending onto the PEDOT:PSS micropillars for both undifferentiated and differentiated SH-SY5Y cells. These membrane protrusions act as sensors of local environment and are, therefore, involved in substrate tethering,[56] suggesting that cells are actively exploring their surroundings. The contact area between differentiated SH-SY5Y cells was further investigated by means of SEM and in situ cross sectioning by FIB milling. Differentiated SH-SY5Y cells tightly adhere to the PEDOT:PSS micropillar electrodes (Figure 4c-iii,iv). The cell membrane is shown to closely follow the substrate surface as the cell is suspended

between two micropillars in B_15 (Figure 4c-iii) or infiltrates in the gap between two micropillars in B_30 (Figure 4c-iv).

The effect of the PEDOT:PSS electrodes' geometry on SH-SY5Y cells differentiation was investigated. After 9 DIV both differentiated (**Figure 5**) and undifferentiated cells (Figure S6, Supporting Information) were fluorescently labelled for nuclei (blue), MAP2 (green), and *β*-III tubulin (red) (Figures S7 and S8, Supporting Information, for the single-channel confocal images). Elongating neurites in differentiated SH-SY5Y cells are shown as they stretch across the substrate while actively exploring their surroundings. The normalized neurite length was significantly different between undifferentiated and differentiated SH-SY5Y cells for each substrate (Figure S9, Supporting Information), suggesting that both PEDOT:PSS flat and micropillar electrodes support SH-SY5Y differentiation. In addition, when the normalized neurite length was compared across all substrates for both differentiated (Figure 5a) and undifferentiated cells (Figure S6b, Supporting Information), no statistical difference was found, suggesting that the
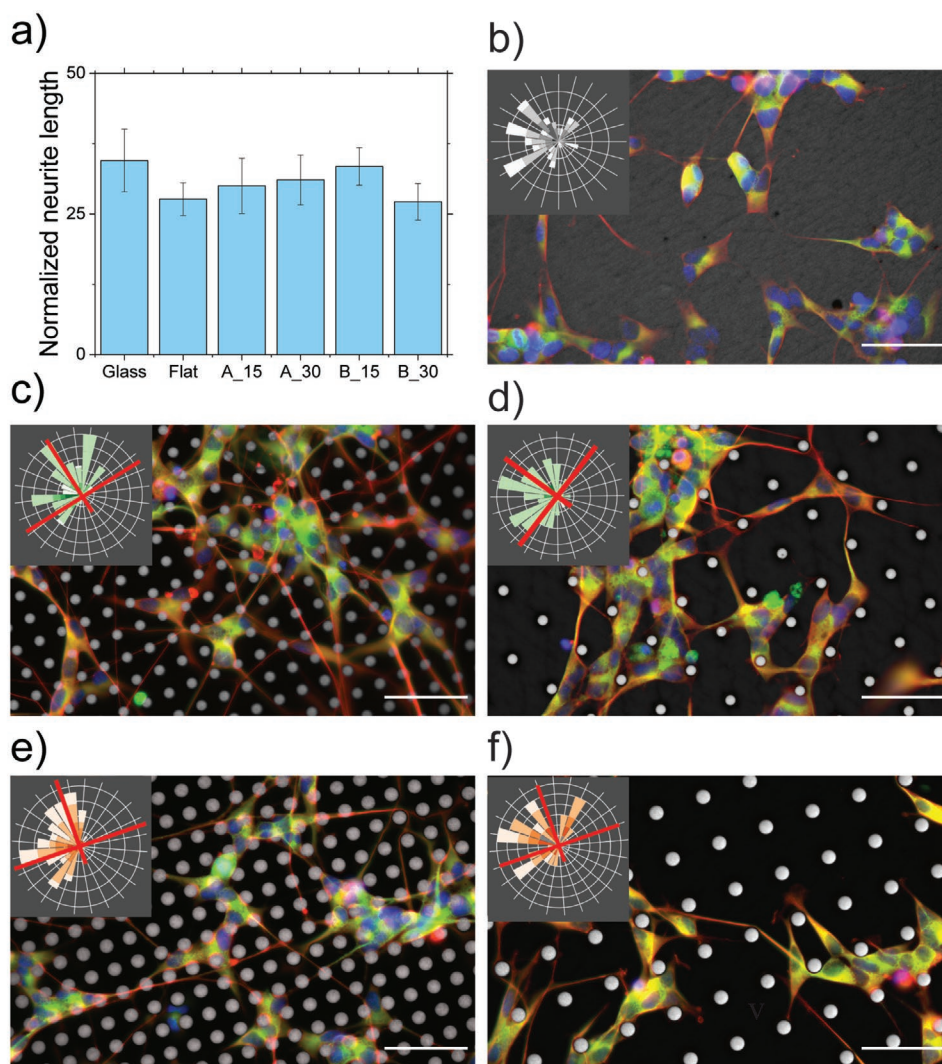
ADVANCED
SCIENCE NEWS
www.advancedsciencenews.com

ADVANCED
MATERIALS
INTERFACES
www.advmatinterfaces.de

Figure 5. The effect of soft PEDOT:PSS micropillars on neurite directionality. a) Normalized neurite length reported as mean ± SD (n = 3); b–f) Fluorescence images of differentiated SH-SY5Y cells on flat (b), A_15 (c), A_30 (d), B_15 (e), and B_30 (f). Cells were fluorescently labelled for the nuclei (blue), MAP2 (green), and β-III tubulin (red). Scale bar 50 µm. The polar plots showing neurite alignment on the 3D_PEDOT arrays are reported in the insets of the corresponding fluorescence image. Crossing red lines are visual guides along the pattern main axes. Divisions refer to neurite counts for image (on average < 50). Higher frequency of neurites in the upper quadrants is due to neurite sampling procedures but has no influence on alignment assessment.

topographical cues provided by the PEDOT:PSS micropillars do not significantly affect the differentiation process. This is in agreement with previous works, suggesting that smaller pillar size and pitch might be required to observe a significant difference in neurite length (both must be between 1 and 2 µm).[57] Vertically aligned topographical cues in the microscale have been used to promote neurite alignment through contact guidance processes at the cell–material interface.[16,17,43,58–60] For this reason, we investigated the potential of our PEDOT:PSS micropillar arrays to guide neurite alignment. Differentiated SH-SY5Y cells fluorescently labelled for β-III tubulin (red) were used for neurite directionality analysis (Figure 5b–f).

The orientation of each neurite within 15° wide sectors was compared with the main direction of the micropillar arrays (Figure 5b–f insets). It is known neurite directionality is influenced by isotropic micropillar arrays with an interpillar distance

below ca. 5 µm.[61] Here, the interpillar distance (along the main pattern direction) is 7.9 and 22.9 µm for A_15 and A_30 and 6.7 and 21.7 µm for B_15 and B_30. Therefore, we could expect that A_15 and B_15 influenced neurite directionality to a major extent compared to A_30 and B_30. Indeed, the most anisotropic neurite orientation was achieved with A_15 and B_15 as the average neurite orientation was highly correlated with the main axis of the pattern (Figure 5b–f insets). Instead, the larger interpillar distance in A_30 and B_30, allowing neurites to freely coordinate their growth, led to directional changes up to 180° with fewer neurites following the pattern main axis direction (**Figure 6**a–c). In this case, micropillars act as anchoring points for the development of neurites, thus helping the generation and the modulation of the traction/tensional forces required for neurite extension. As previously reported, cells adhere and migrate on micropillar arrays by applying traction
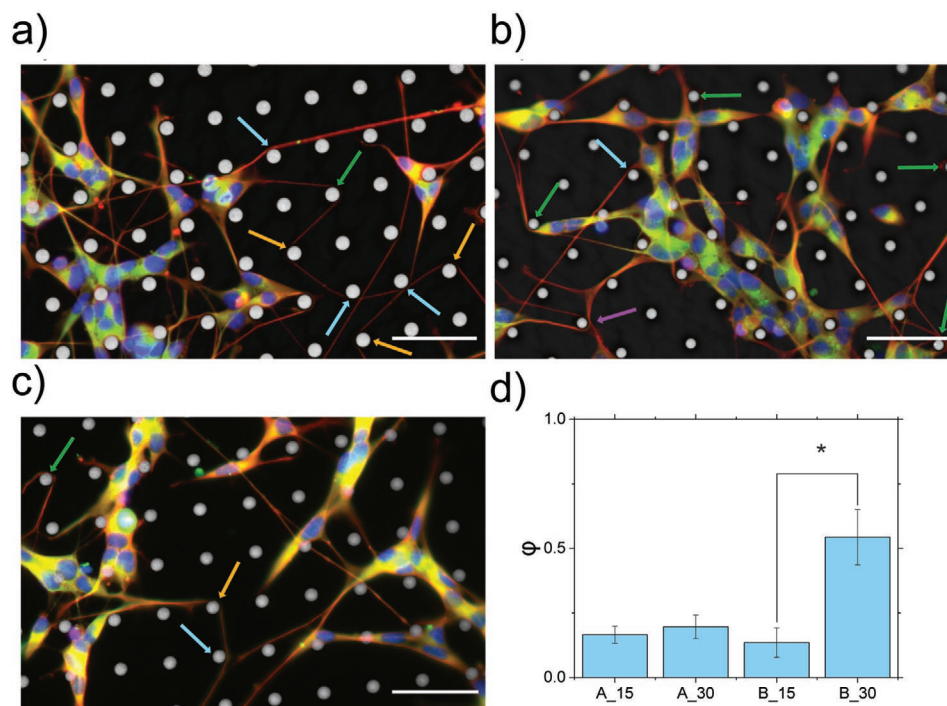
Figure 6. Tensioning of neurites around micropillars in low-density 3D_PEDOT. a–c) Exemplary fluorescence images of differentiated SH-SY5Y cells on B_30 (a) and A_30 (b,c). Cells were fluorescently labelled for the nuclei (blue), MAP2 (green) and β-III tubulin (red). The angle of direction change of a neurite around a micropillar (ϑ) around micropillars are indicated by colored arrows (light blue for $\vartheta < 90°$; yellow for ϑ ca. 90°, green for $90° < \vartheta < 180°$, violet ϑ ca. 180°. Scale bar 50 µm. d) The density of deflection points per total number of neurites (φ) is plotted for each type of array. The variable number of neurites in the images contributes to statistical variance in the cumulative histograms.

forces through their interaction with the pillar surface.[15,62] Figure 6d shows the correlation between the fraction of deflection points (i.e., the number of pillars that deflect neurites per total number of neurites) and the pillar arrays. The most significant effect was found for B_30, suggesting that a larger pillar diameter and a larger interpillar distance offer more accessible anchoring points for neurites compared to denser arrays with smaller pillars.

3. Conclusions

Flexible conductive microarrays are attractive for the manufacturing of next-generation flexible stretchable electronic devices and sensors. Here, we demonstrated a simple approach for fabricating microstructured 3D electrodes of PEDOT:PSS on a PDMS substrate. We combined replica molding and electrodeposition to provide soft PEDOT:PSS micropillars with tunable electrical properties, in particular capacitance and ESA. Notably, the presence of the PEDOT:PSS layer provided a nanostructured and moderately hydrophobic surface, both beneficial features for cell adhesion. Indeed, undifferentiated and differentiated SH-SY5Y cells adhered and spread on the PEDOT:PSS micropillar arrays, tightly interacting with the soft micropillars. Upon differentiation, the directionality of neurite extension was influenced by the geometry of the micropillar array with complex responses induced by the micropillars and their periodicity. Overall, we have successfully developed a straightforward

fabrication process for the fabrication of soft PEDOT:PSS micropillars as promising 3D electrodes for bioelectronics application.

4. Experimental Section

Fabrication of the Micro-Hole Textured Silicon Masters: Microhole textured silicon masters were obtained recurring to a multi-step fabrication process. In detail, a 50 nm thick Cr layer was deposited onto a P-type Si wafer by 48W constant power DC sputtering (Kenosistec Confocal Sputter Coater KS500). Optical lithography (Heidelberg DWL66FS laser writer system) was employed to define a square lattice microhole array onto the AZ 5214E image reversal photoresist (MicroChemicals GmbH, Germany) previously deposited via spin-coating at 4000 rpm and baked at 120 °C for 1 min. Nominal microhole dimensions were as follows: 5 and 7 µm (diameter), 3 µm (hole depth), and 15 and 30 µm (pitch). The exposed resist was developed in a conventional AZ 726 MIF solution for 1 min, while the underlying Cr film was selectively (i.e., within the textured areas) removed in standard etchant solution (Chrome etch 18, MicroResist Technology GmbH). Afterward, the unexposed resist was completely dissolved in Acetone, yielding a Cr-mask for the subsequent ion etching step. The microhole pattern was indeed realized in a Sentech SI500 ICP-RIE system, exploiting a Bosch-like process. The etched depth and the side walls verticality were optimized by carefully tuning the isotropic SF_6 plasma cycle parameters (SF_6 129 sccm, Ar 5 sccm, RF power 40 W, ICP power 100 W, temperature 0 °C, etching rate 150 nm/cycle). Finally, the residual Cr-mask was entirely removed by means of the etchant solution.

Fabrication of the 3D_PEDOT Arrays: Replica molding (RM) method was applied to obtain high-fidelity negative replica of the microhole

textured master. PDMS was prepared by Sylgard 184 Silicon Elastomer Base and Sylgard 184 Elastomer Base Curing Agent (Dow Europe GmbH, Horgen, Switzerland) in a 10:1 (v/v) ratio. The mixture was degassed in vacuum, poured on the silicon masters, and cured overnight at 60 °C. Subsequently, the free-standing PDMS replicas were gently lift off and placed on a stainless-steel foil support for the metallization step. The surface of the PDMS substrates was metallized under high vacuum conditions (working pressure: 8×10^{-7} mbar) by evaporating the metals with thermo Joule sources. The bulk titanium and gold (Gold and Titanium evaporation slug 3×3 mm purity $\geq 99.99\%$ Sigma-Aldrich, MO, USA were charged in two independent tungsten boats and the evaporation rate was monitored with a quartz microbalance. Ca. 3 nm of titanium (Ti) were evaporated directly on PDMS with a very slow evaporation rate (0.1 Å s^{-1}) and acted as adhesion layer. Then, ca. 35 nm layer of gold (Au) were deposited on the titanium (evaporation rate 2 Å s^{-1}), forming a conductive metallic layer. PEDOT:PSS thin films (thickness between 300 and 400 nm, see Table S2, Supporting Information) were electrodeposited on the surface of the metallized micropillared PDMS substrates in a three-electrodes cell A, using a large-area platinum foil (15×5 mm^2) as counter electrode and a standard Ag|AgCl (3 M KCl) as reference electrode. The metallized PDMS substrates were contacted with Ag conductive paste and set as working electrode. A solution of 3,4-Ethylenedioxythiophene (EDOT, 0.01 M, Sigma Aldrich, MO, USA) in aqueous polysulfate sodium (NaPSS, 0.7% w/w, Sigma Aldrich, MO, USA) was used for the electrochemical deposition upon sweeping the potential between 0 and +1 V for 15 cycles.

Surface Characterization of the 3D_PEDOT: Optical Microscopy (LEICA Steromicroscope M205 FA, Leica Microsystems, Vienna, Austria) was used to evaluate the reproducibility/accuracy of the different fabrication steps and spot defects on macroscopic scale lengths. SEM was used to evaluate characteristic geometrical features of the silicon masters and the PDMS replica, of the Ti—Au/PDMS and of the 3D_PEDOT on microscopic scale lengths. A SEM ZEISS EVO40 XPV (Carl Zeiss GmbH, Oberkochen, Germany) was operated at 15 kV acceleration voltage. PDMS samples were coated with a ≈5 nm of gold before acquisition. Some images were acquired using a tilt angle of ≈45°. Atomic force microscopy (AFM) was used to both analyze surface topography at the nanoscale and measure the thickness of the electrodeposited PEDOT:PSS layers. Images were acquired in air at room temperature using a Park XE7 atomic force microscopy (AFM) System (Park System, Suwon, Korea) operating in non-contact mode. Pre-mounted silicon cantilever with backside reflecting coating (Al), typical tip curvature radius ≈7 nm, $k \approx 26$ N m^{-1} and resonance frequency ≈300 kHz were used (OMCL-AC160TS, Olympus Micro Cantilevers, Tokyo, Japan). The RMS of PDMS, Ti—Au/PDMS, and 3D PEDOT were extracted from several topography images acquired at different scan size using the Park Systems XEI Software (Park Systems, Suwon, Korea). The thicknesses of PEDOT:PSS films were calculated by extracting the height profile across microcracks present in the PEDOT:PSS film due to the different mechanical properties of PDMS and Au, considering at least three different representative images for sample. Contact angle measurements were carried out to evaluate the wettability of the 3D PEDOT micropillar arrays using a home-built contact angle measurement unit. The value of the water contact angle was obtained by averaging several measurements of the left and right contact angle of the milliQ water drop taken on different areas of the samples by using the ImageJ free software (https://imagej.nih.gov/)

Electrochemical Characterization of the 3D_PEDOT Electrodes: All electrochemical measurements were performed in saline solution (NaCl$_{aq}$ 0.15 M), with the same setup described for the electrochemical deposition process. Electrochemical capacitance (C) of the 3D_PEDOT electrodes was extracted by cyclic voltammetry (CV) curves acquired at a different scan rate ν (20/40/60/80 mV s^{-1}), sweeping the potential between 0 and 0.6 V, by means of the following expression:

$$I_{cat} = C\nu \tag{1}$$

The cathodic current (I_{cat}) values were chosen in the plateau region at $V = 0.3$ V. The ESA was extracted by an independent set of CVs performed in a solution of 10^{-4} M Ru(NH$_3$)$_6$Cl$_3$ in saline. ESA values were obtained by using the Randles–Sevcik Equation (2) which relates the peak current of the electron-transfer-controlled process with the square root of the scan rate.

$$I_p = 2.69\,10^5\,n^{3/2}\,\text{ESA}\,D^{1/2}S\nu^{1/2} \tag{2}$$

where I_p is the peak current, n is the number of transfer electrons, D is the diffusion coefficient in centimeter square per second, S is the concentration of the electroactive species in mole per centimeter cube (1000 times molarity) and ν is the scan rate in millivolts per second. The diffusion coefficient of Ru(NH$_3$)$_6$Cl$_3$ (D = 1.13 10^5 cm^2 s^{-1}) was obtained from an independent set of CVs using a gold electrode of known diameter and plotting the peak current I_p against the scan rate square root $\nu^{1/2}$. The constant in front of Equation (1) has the proper physical dimensions.

Cell Culture and Differentiation Protocol: SH-SY5Y neuroblastoma cells were cultured in Dulbecco's Modified Eagle's Medium/Nutrient Mixture F-12 Ham (Sigma-Aldrich) supplemented with 10% of fetal bovine serum (Life Technologies), 1% Ala-gln (200 mM, Sigma-Aldrich) and 1% of penicillin-streptomycin (10 000 U mL^{-1}, Sigma-Aldrich). For the differentiation experiments, cells were trypsinized using warm 1 mL of Trypsin-EDTA (0.25%, Life Technologies) for 5 min. After quenching the trypsin by adding 5 mL of warm standard medium, cells were centrifuged for 5 min at 1000 rpm. The supernatant was removed without disturbing the pellet. The pellet was then resuspended in 5 mL of culture media and a 50 µL drop containing 21 000 cells was plated on each substrate. At DIV 1, the standard medium was replaced with a differentiation media containing Dulbecco's Modified Eagle's Medium/Nutrient Mixture F-12 Ham (Sigma-Aldrich) supplemented, 1% Ala-gln (200 mM, Sigma-Aldrich), 1% of penicillin-streptomycin (10 000 U mL^{-1}, Sigma-Aldrich) and 1 µM Retinoic acid. At DIV 4, the medium was replaced again with a new differentiation media containing Dulbecco's Modified Eagle's Medium/Nutrient Mixture F-12 Ham (Sigma-Aldrich) supplemented, 1% Ala-gln (200 mM, Sigma-Aldrich), 1% of penicillin-streptomycin (10 000 U mL^{-1}, Sigma-Aldrich) and 0.2 µg mL^{-1} Brain derived Neurotrophic factor (BDNF). At DIV7, cells were switched to neurons media containing Neurobasal-A Medium (Life technologies) supplemented with 1% B-27 supplement (Thermofisher scientific), 0.25% Ala-gln (200 mM, Sigma-Aldrich), and 0.1% penicillin-streptomycin (10 000 U mL^{-1}, Sigma-Aldrich).

Live/Dead Assay: Cells were gently seeded on each substrate at a density of 80 000 cells cm^{-2} and incubated at 37 °C with 5% CO$_2$. Cytotoxicity was evaluated after 1 DIV. Calcein-AM (Sigma-Aldrich) and ethidium homodimer (Abcam) were used to fluorescently label live and dead cells, respectively. The staining solution containing 1 µg mL^{-1} Calcein AM and 1 µg mL^{-1} ethidium homodimer was added to cells and incubated for 15 min at 37 °C. Samples were rinsed in PBS and mounted on glass coverslips for imaging. All the fluorescence images for the live/dead assay were taken using this microscope (Axio Imager Z2 Vario, Zeiss) using an N-Achroplan 20×/0.5 water objective with an additional Optovar 1.6× magnification. Numbers of live and dead cells were estimated using the "Find Maxima" command on ImageJ. The percentage of live cells was measured using the following formula:

$$\% \text{ Viability} = \frac{(\text{Live cells})}{(\text{Live cells} + \text{Dead cells})} \times 100 \tag{3}$$

Immunocytochemistry: Both differentiated and undifferentiated cells were fixed at DIV 9 in 4% paraformaldehyde (PFA) in PBS for 20 min at room temperature and then washed three times with 1× PBS. Cells were permeabilized with 0.1% Triton-X 100 (Sigma-Aldrich) in 1× PBS for 5 min and then incubated in a blocking solution containing 2% bovine serum albumin (BSA, Sigma-Aldrich) for 45 min at room temperature. Cells were labelled with microtubule-associated protein (MAP2) rabbit polyclonal antibody (1:200, SYSY) and for β-III tubulin mouse

2200709 (9 of 11)

**ADVANCED
SCIENCE NEWS**

www.advancedsciencenews.com

**ADVANCED
MATERIALS
INTERFACES**

www.advmatinterfaces.de

monoclonal antibody (1:200, Abcam). Both antibodies were diluted in 1% BSA in 1× PBS and incubated with cells for 60 min at room temperature. Samples were washed three times in 1% BSA in 1× PBS and labelled with Alexa Fluor 488 goat anti-rabbit secondary antibody (1:500, Abcam) and Alexa Fluor 647 goat anti-mouse secondary antibody (1:500, Invitrogen). Both antibodies were diluted in in 1% BSA in 1× PBS for 60 min at room temperature; cells were then washed three times in 1% BSA in PBS. Cell nuclei were stained with Hoechst in 1% BSA in 1× PBS (1:5000, Life Technologies) for 10 min at room temperature. Samples were washed three times in 1× PBS and imaged. All the fluorescence images for the immunocytochemistry were taken using this microscope (Axio Imager Z2 Vario, Zeiss) using an N-Achroplan 40×/0.75 water objective with an additional Optovar 1.6× magnification. Number of cells and neurite length were measured using ImageJ. The normalized neurite length was calculated using the following formula:

$$Normalized\ neurite\ length = \frac{Total\ neurite\ length}{Number\ of\ cells} \qquad (4)$$

Statistical Analysis: For the viability and normalized neurite length, all the data is plotted as mean ± SEM. The statistical analysis was performed using GraphPad Prims 8. A One-way Anova test followed by a Dunnett's post hoc analysis was performed to assess any effect of the substrates used on the percentage of live cells compared to glass. The same statistical analysis was performed to assess any substrate-induced effect on cell differentiation. To compare the normalized neurite length between differentiated and undifferentiated cells for each substrate, an unpaired Student's *t*-test was used.

Specimens' Resin Embedding: Cells for SEM imaging were treated following the ultrathin plasticization method.[63] At 9 DIV both undifferentiated and differentiated cells were fixed in 2.5% glutaraldehyde (Electron Microscopy Science) diluted in 0.1 M sodium cacodylate buffer (Electron Microscopy Science) for 60 min at room temperature and then washed three times for 5 min with buffer at 4 °C. Buffer solution was then replaced with 20 mM glycine (Sigma-Aldrich) in 0.1 M sodium cacodylate buffer. After 3 × 5 min washes in 0.1 sodium cacodylate washes, samples were incubated with 2% osmium tetroxide (Electron Microscopy Science) reduced by 2% potassium ferrocyanide (Electron Microscopy Science) for 60 min at 4 °C. Samples were then immersed in 1% filtered thiocarbohydrazide (Electron Microscopy Science) in DI water for 20 min at room temperature, washed 3 × 5 min in DI water, and incubated overnight in 4% filtered uranyl acetate at 4 °C. Radioactive solution was removed and replaced with first DI water and then 0.15% tannic acid (Sigma-Aldrich) diluted in DI water for 3 min. Afterward, samples were gradually dehydrated with an ascending series of ethanol dilutions (30%, 50%, 75%, 95%, and 100% v/v ethanol in water) for 10 min each at 4 °C. Ethanol 100% was exchanged two times at room temperature prior sample inclusion in resin ((Electron Microscopy Science) which occurs gradually with an ethanol:resin ratio 1:3 for 3 h, 1:1 overnight and absolute resin for at least other 8 h. Minimal resin covering on the cells was achieved by upright positioning the samples and let the resin drain by gravity for 2 h. Resin was finally polymerized in the oven at 70 °C for 12 h. Samples were mounted onto aluminum stubs (diameter: 3.2 mm) using silver conductive paste (RS Pro) and were then sputtered with 10–40 nm thick golden layer prior to imaging.

Scanning Electron Microscopy Imaging and Focused Ion Beam Milling: Samples were loaded inside the dual-beam chamber (G4, ThermoFisher) and a region of interest located. Platinum was deposited in two steps at the region of interest through electron-assisted deposition (0.5 µm thickness at 3 kV and 0.69–2.7 nA) and a subsequent ion-assisted deposition (≈1 µm thickness at 30.0 kV and 0.79 nA). Cross sections were realized by first trenching out the material via ion beam (≈5 µm nominal depth for Si 30 kV and 0.25–9.3 nA) and then by polishing the interface with the ion beam (≈1 µm nominal depth for Si, 30.0 kV and 80 pA to 0.23 nA). SEM images were acquired in backscattered mode fixing dwell time at 30 µs and the electron beam parameters to 2.0 kV and 86 pA to 2.8 nA.

Analysis of Neurite Alignment: The position of advancing neurites had been traced with coordinates of consecutive segments approximating the shape of the neural process. Only neurites and processes clearly

distinguishable were recorded for the analysis, excluding cell connections arising from the 3D growth of cell aggregates. The tracing analysis had been performed using NeuronJ plugin on ImageJ. The orientation of the segment joining the starting and final points of neuron processes, within 15° wide sectors, was compared with the main direction of the pattern, with histograms in polar coordinates, that report in color scale the length of PEDOT pillars. The analysis of alignment was performed with package circular of statistics software R.[64] The fraction of deflection points on each array was expressed as:

$$\varphi = number\ of\ pillars\ deflecting\ neurites/total\ number\ of\ neurites \qquad (5)$$

Supporting Information

Supporting Information is available from the Wiley Online Library or from the author.

Acknowledgements

Conflict of Interest

The authors declare no conflict of interest.

Data Availability Statement

The data that support the findings of this study are available from the corresponding author upon reasonable request.

Keywords

[1] L. D. Garma, L. Matino, G. Melle, F. Moia, F. D. Angelis, F. Santoro, M. Dipalo, *PLoS One* **2019**, *14*, e0214017.

[2] M. E. J. Obien, K. Deligkaris, T. Bullmann, D. J. Bakkum, U. Frey, *Front. Neurosci.* **2015**, *8*, 423.

[3] B. C. Wheeler, Y. Nam, *Crit. Rev. Bioeng.* **2011**, *39*, 45.

[4] R. Kim, S. Joo, H. Jung, N. Hong, Y. Nam, *Biomed. Eng. Lett.* **2014**, *4*, 129.

[5] A. Mariano, C. Lubrano, U. Bruno, C. Ausilio, N. B. Dinger, F. Santoro, *Chem. Rev.* **2022**, *122*, 4552.

[6] C. Simitzi, A. Ranella, E. Stratakis, *Acta Biomater.* **2017**, *51*, 21.

[7] I. Tonazzini, E. Bystrenova, B. Chelli, P. Greco, P. Stoliar, A. Calò, A. Lazar, F. Borgatti, P. D'Angelo, C. Martini, F. Biscarini, *Biophys. J.* **2010**, *98*, 2804.

[8] T. Cramer, B. Chelli, M. Murgia, M. Barbalinardo, E. Bystrenova, D. M. de Leeuw, F. Biscarini, *Phys. Chem. Chem. Phys.* **2013**, *15*, 3897.

[9] B. Chelli, M. Barbalinardo, F. Valle, P. Greco, E. Bystrenova, M. Bianchi, F. Biscarini, *Interface Focus* **2014**, *4*, 20130041.

[10] M. E. Spira, A. Hai, *Nat. Nanotechnol.* **2013**, *8*, 83.

[11] J. T. Robinson, M. Jorgolli, A. K. Shalek, M.-H. Yoon, R. S. Gertner, H. Park, *Nat Nanotechnol.* **2012**, *7*, 180.

[12] J. Yoo, H. Kwak, J. Kwon, G. E. Ha, E. H. Lee, S. Song, J. Na, H.-J. Lee, J. Lee, A. Hwangbo, E. Cha, Y. Chae, E. Cheong, H.-J. Choi, *Sci. Rep.* **2020**, *10*, 4279.

[13] R. Liu, R. Chen, A. T. Elthakeb, S. H. Lee, S. Hinckley, M. L. Khraiche, J. Scott, D. Pre, Y. Hwang, A. Tanaka, Y. G. Ro, A. K. Matsushita, X. Dai, C. Soci, S. Biesmans, A. James, J. Nogan, K. L. Jungjohann, D. V. Pete, D. B. Webb, Y. Zou, A. G. Bang, S. A. Dayeh, *Nano Lett.* **2017**, *17*, 2757.

[14] O. Staufer, S. Weber, C. P. Bengtson, H. Bading, A. Rustom, J. P. Spatz, *Nano Lett.* **2019**, *19*, 3244.

[15] Y. Alapan, K. Icoz, U. A. Gurkan, *Biotechnol. Adv.* **2015**, *33*, 1727.

[16] N. M. Dowell-Mesfin, M.-A. Abdul-Karim, A. M. P. Turner, S. Schanz, H. G. Craighead, B. Roysam, J. N. Turner, W. Shain, *J. Neural Eng.* **2004**, *1*, 78.

[17] A. Cutarelli, S. Ghio, J. Zasso, A. Speccher, G. Scarduelli, M. Roccuzzo, M. Crivellari, N. M. Pugno, S. Casarosa, M. Boscardin, L. Conti, *Cells* **2019**, *9*, 88.

[18] R. Akhtar, M. J. Sherratt, J. K. Cruickshank, B. Derby, *Mater. Today* **2011**, *14*, 96.

[19] G. Hong, C. M. Lieber, *Nat. Rev. Neurosci.* **2019**, *20*, 330.

[20] R. A. Green, R. T. Hassarati, J. A. Goding, S. Baek, N. H. Lovell, P. J. Martens, L. A. Poole-Warren, *Macromol. Biosci.* **2012**, *12*, 494.

[21] M. Bianchi, A. De Salvo, M. Asplund, S. Carli, M. Di Lauro, A. Schulze-Bonhage, T. Stieglitz, L. Fadiga, F. Biscarini, *Adv. Sci.* **2022**, *9*, 2104701.

[22] A. Maziz, E. Özgür, C. Bergaud, L. Uzun, *Sens. Actuators Rep.* **2021**, *3*, 100035.

[23] J. Rivnay, R. M. Owens, G. G. Malliaras, *Chem. Mater.* **2014**, *26*, 679.

[24] P. Yin, Y. Liu, L. Xiao, C. Zhang, *Polymers* **2021**, *13*, 2834.

[25] C. Boehler, S. Carli, L. Fadiga, T. Stieglitz, M. Asplund, *Nat. Protoc.* **2020**, *15*, 3557.

[26] S. Carli, M. Bianchi, E. Zucchini, M. Di Lauro, M. Prato, M. Murgia, L. Fadiga, F. Biscarini, *Adv. Healthcare Mater.* **2019**, *8*, 1900765.

[27] M. Di Lauro, A. De Salvo, G. C. Sebastianella, M. Bianchi, S. Carli, M. Murgia, L. Fadiga, F. Biscarini, *ACS Appl. Electron. Mater.* **2020**, *2*, 1849.

[28] X. T. Cui, D. D. Zhou, *IEEE Trans. Neural Syst. Rehabil. Eng.* **2007**, *15*, 502.

[29] C. Boehler, M. Asplund, in 2018 40th Ann. Int. Conf. IEEE Eng. Med. Biol. Soc. (EMBC), IEEE, Honolulu, HI **2018**, pp. 2202.

[30] A. S. Pranti, A. Schander, A. Bödecker, W. Lang, *Sens. Actuators, B* **2018**, *275*, 382.

[31] G. Tullii, F. Giona, F. Lodola, S. Bonfadini, C. Bossio, S. Varo, A. Desii, L. Criante, C. Sala, M. Pasini, C. Verpelli, F. Galeotti, M. R. Antognazza, *ACS Appl. Mater. Interfaces* **2019**, *11*, 28125.

[32] F. Milos, G. Tullii, F. Gobbo, F. Lodola, F. Galeotti, C. Verpelli, D. Mayer, V. Maybeck, A. Offenhäusser, M. R. Antognazza, *ACS Appl. Mater. Interfaces* **2021**, *13*, 23438.

[33] Y. Liu, A. F. McGuire, H.-Y. Lou, T. L. Li, J. B.-H. Tok, B. Cui, Z. Bao, *Proc. Natl. Acad. Sci. USA* **2018**, *115*, 11718.

[34] I. Bernardeschi, F. Greco, G. Ciofani, A. Marino, V. Mattoli, B. Mazzolai, L. Beccai, *Biomed. Microdevices* **2015**, *17*, 46.

[35] J. Li, W. Tang, Q. Wang, W. Sun, Q. Zhang, X. Guo, X. Wang, F. Yan, *Mater. Sci. Eng.: R: Rep.* **2018**, *127*, 1.

[36] X. Fan, W. Nie, H. Tsai, N. Wang, H. Huang, Y. Cheng, R. Wen, L. Ma, F. Yan, Y. Xia, *Adv. Sci.* **2019**, *6*, 1900813.

[37] B. Guo, L. Glavas, A.-C. Albertsson, *Prog. Polym. Sci.* **2013**, *38*, 1263.

[38] R. Song, M. Murphy, C. Li, K. Ting, C. Soo, Z. Zheng, *Drug Des Devel Ther.* **2018**, *12*, 3117.

[39] A. Campana, T. Cramer, P. Greco, G. Foschi, M. Murgia, F. Biscarini, *Appl. Phys. Lett.* **2013**, *103*, 073302.

[40] A. Campana, T. Cramer, D. T. Simon, M. Berggren, F. Biscarini, *Adv. Mater.* **2014**, *26*, 3873.

[41] R. Boni, A. Ali, A. Shavandi, A. N. Clarkson, *J. Biomed. Sci.* **2018**, *25*, 90.

[42] L. Sordini, F. F. F. Garrudo, C. A. V. Rodrigues, R. J. Linhardt, J. M. S. Cabral, F. C. Ferreira, J. Morgado, *Front. Bioeng. Biotechnol.* **2021**, *9*, 73.

[43] M. Mattotti, L. Micholt, D. Braeken, D. Kovačić, *J. Neural Eng.* **2015**, *12*, 026001.

[44] E. Tamburri, S. Orlanducci, F. Toschi, M. L. Terranova, D. Passeri, *Synth. Met.* **2009**, *159*, 406.

[45] M. Ventre, F. Valle, M. Bianchi, F. Biscarini, P. A. Netti, *Langmuir* **2012**, *28*, 714.

[46] G. Graziani, M. Berni, A. Gambardella, M. De Carolis, M. C. Maltarello, M. Boi, G. Carnevale, M. Bianchi, *Mater. Sci. Eng., C* **2019**, *99*, 853.

[47] V.-Q. Nguyen, D. Schaming, P. Martin, J.-C. Lacroix, *ACS Appl. Mater. Interfaces* **2015**, *7*, 21673.

[48] D. Qi, K. Zhang, G. Tian, B. Jiang, Y. Huang, *Adv. Mater.* **2021**, *33*, 2003155.

[49] Q. Yu, F. Chen, M. Li, H. Cheng, *Appl. Phys. Lett.* **2017**, *111*, 121904.

[50] D. A. Koutsouras, P. Gkoupidenis, C. Stolz, V. Subramanian, G. G. Malliaras, D. C. Martin, *ChemElectroChem* **2017**, *4*, 2321.

[51] J. Bobacka, A. Lewenstam, A. Ivaska, *J. Electroanal. Chem.* **2000**, *489*, 17.

[52] S. F. Cogan, *Annu. Rev. Biomed. Eng.* **2008**, *10*, 275.

[53] M. Bianchi, S. Carli, M. Di Lauro, M. Prato, M. Murgia, L. Fadiga, F. Biscarini, *J. Mater. Chem. C* **2020**, *8*, 11252.

[54] H. He, L. Zhang, X. Guan, H. Cheng, X. Liu, S. Yu, J. Wei, J. Ouyang, *ACS Appl. Mater. Interfaces* **2018**, *11*, 26185.

[55] B. Guo, P. X. Ma, *Biomacromolecules* **2018**, *19*, 1764.

[56] C. A. Heckman, H. K. Plummer, *Cell. Signalling* **2013**, *25*, 2298.

[57] L. Micholt, C. Bartic, *PLoS One* **2013**, *8*, e66170.

[58] C. Simitzi, P. Efstathopoulos, A. Kourgiantaki, A. Ranella, I. Charalampopoulos, C. Fotakis, I. Athanassakis, E. Stratakis, A. Gravanis, *Biomaterials* **2015**, *67*, 115.

[59] J. N. Hanson, M. J. Motala, M. L. Heien, M. Gillette, J. Sweedler, R. G. Nuzzo, *Lab Chip* **2009**, *9*, 122.

[60] G. S. Lorite, L. Ylä-Outinen, L. Janssen, O. Pitkänen, T. Joki, J. T. Koivisto, M. Kellomäki, R. Vajtai, S. Narkilahti, K. Kordas, *Nano Res.* **2019**, *12*, 2894.

[61] M. Park, E. Oh, J. Seo, M.-H. Kim, H. Cho, J. Y. Choi, H. Lee, I. S. Choi, *Small* **2016**, *12*, 1148.

[62] L. Trichet, J. Le Digabel, R. J. Hawkins, S. R. K. Vedula, M. Gupta, C. Ribrault, P. Hersen, R. Voituriez, B. Ladoux, *Proc. Natl. Acad. Sci. U. S. A.* **2012**, *109*, 6933.

[63] F. Santoro, W. Zhao, L.-M. Joubert, L. Duan, J. Schnitker, Y. van de Burgt, H.-Y. Lou, B. Liu, A. Salleo, L. Cui, Y. Cui, B. Cui, *ACS Nano* **2017**, *11*, 8320.

[64] S. Tortorella, P. Greco, F. Valle, M. Barbalinardo, G. Foschi, F. Lugli, M. Dallavalle, F. Zerbetto, C. A. Bortolotti, F. Biscarini, *Bioprinting* **2022**, *26*, e00194.